Journal of Power Sources 196 (2011) 2046–2054

Contents lists available at ScienceDirect

Journal of Power Sources

journal homepage: www.elsevier.com/locate/jpowsour

Microstructure of porous composite electrodes generated by the discrete element method

Xiaoxing Liu[a], Christophe L. Martin[a,*], Gérard Delette[b], Jérome Laurencin[b], Didier Bouvard[a], Thibaud Delahaye[b]

[a] Laboratoire SIMAP - GPM2, Grenoble INP, UJF - CNRS 101, rue de la physique - BP46 38402 Saint Martin d'Hères cedex, France
[b] CEA-Grenoble, DRT/LITEN, 17 rue des Martyrs, 38054 Grenoble Cedex 9, France

ARTICLE INFO

Article history:
Received 8 June 2010
Received in revised form 30 August 2010
Accepted 16 September 2010
Available online 20 October 2010

Keywords:
Sintering
SOFC
Discrete simulation

ABSTRACT

Typical microstructures of LSM/YSZ, NiO/YSZ, Ni/YSZ composite electrodes are simulated by the discrete element method. The numerical microstructures are generated by taking into account in a realistic manner the sintering process. This allows complex microstructures such as bilayers or microstructures containing pore formers to be obtained. NiO particles in the NiO/YSZ composite electrodes are reduced to Ni. Reduction is carried out with the discrete element formalism which allows particle rearrangement to be taken into account. We show that the mechanical percolation of the YSZ phase plays an important role during the reduction of NiO. The various numerical microstructures generated by sintering and reduction are analyzed to evaluate important microstructural features such as macroscopic porosity, pore surface area and Triple Phase Boundary length.

1. Introduction

Electrochemical performance of an SOFC (Solid Oxide Fuel Cell) or SOEC (Solid Oxide Electrolysis Cell) strongly depends on the microstructure of the porous electrodes which constitute the most critical element of the cell. Electrodes are fabricated from ceramic powders that are partially sintered to obtain a functionalized porous ceramic. Taking advantage of the freedom in microstructure design that powder processes allow, experimentalists have proposed various microstructural architectures for porous electrodes. They have well established the strong dependence of the functional properties of a porous ceramic, at a fixed chemical composition, on microstructure [1–6].

Thus, a number of studies have demonstrated that gains may be obtained by improving the microstructure of the porous electrodes for a given cathode or anode material. The main goal of improving the microstructural design is to lower the operating temperature without decreasing the power densities. For example, the fuel cell program of Forschungszentrum Jülich developed so-called functional layers, both at the cathode/electrolyte interface and at the anode substrate/electrolyte interface [3]. In that case the cathode functional layer is a composite made of a mixture of electronic and ionic conducting particles which allows a large increase of the number of active sites. The use of fine-grained microstructure also increases the number of so-called Three-Phase Boundary (TPB) per unit volume. Typically submicron sized powders (provided they do not experience too large a coarsening during sintering) are expected to produce larger TPB length per unit volume of electrode [7,8]. Other examples of enhanced microstructures deal with the control of the pore architecture both for anodes and cathodes [5,9] and with the possibility of grading porosity along the thickness of the electrodes [10,11]. Control of porosity and pore architecture has been demonstrated with various types of pore formers in electrode fabrication [5,8,9,12]. Pore formers are used to adjust the shrinkage of each layer during the co-sintering stage of multi-layered electrodes but may also be used to enhance, under operation, the diffusion of gaseous species to the functional layers [12,13].

These examples, using very different routes for optimizing electrodes, show that it is critical to gain a more thorough understanding of the correlation between the microstructure at the length scale of powder particles and the macroscopic electrode performances. Also, linking pertinent microstructural features to the macroscopic behavior would allow predictive models to guide the design of optimized microstructural architectures.

Since most routes for fabricating electrodes involve depositing a powder mixture onto a dense electrolyte and then sintering this mixture, such models should be able to reproduce these steps with some accuracy. This would allow mimicking the complex microstructural designs produced by powder processing. However, such a modeling approach requires an integrated approach of the electrode processing from the initial powders to the final porous electrode. Thus, any model of the electrode microstructure

---

* Corresponding author. Tel.: +33 476826337; fax: +33 476826382.
E-mail address: Christophe.Martin@grenoble-inp.fr (C.L. Martin).

0378-7753/$ – see front matter © 2010 Elsevier B.V. All rights reserved.
doi:10.1016/j.jpowsour.2010.09.033

needs to acknowledge the particulate nature of the material which has been processed to obtain the final electrode. This has been only partially recognized by analytical models which compute for example TPB length as a function of porosity, particle size and composition [14–17]. These analytical models have the advantage of demonstrating in a simple and elegant way the effect of the main parameters which control the TPB length. However, the microstructure is still modeled in a very approximate manner and the sintering process is treated only through its effect on the decrease of the macroscopic porosity.

Other models use numerical microstructures to mimic the porous electrodes. These numerical simulations use a random packing of spheres which indent each other to create a porous material. The contacts between electronic and ionic conducting particles allow the TPB length to be computed for various compositions and electrode thicknesses [18,19], particle sizes [20] and particle size distributions [21] and composition gradients [22]. Using image analysis techniques, it is also possible to obtain from these numerical microstructures other important microstructural features such as pore size and geometry and pore percolation threshold [21,23]. From these microstructural features and from the intrinsic conductive properties of the particles, it is then possible to compute the effective electric and electrochemical properties of the electrodes by assuming that current is conducted at solid bonds between particles [14,17,18,20,22,24,25].

All these models recognize the particulate (or discrete) nature of the porous electrode and have improved our understanding of the effect of important features such as percolation, electrode thickness, composition and particle size. However, they are still a very approximate picture of the real microstructure. In particular in most of these models, the sintering process is treated simply as the growth of particle radii to form solid bonds between particles [17,20,21,24,25], thus neglecting particle rearrangement that must occur at interfaces with the dense electrolyte or when a mixture of particles with different sizes is used. Also, the reduction of the NiO ceramic into metallic Ni to form a cermet anode is not treated in terms of its microstructural consequences. For example Golbert et al. have treated the reduction of NiO and the resulting increase in porosity by introducing numerically pore formers which are subsequently removed [20]. The most advanced models on reduction of NiO to Ni (and subsequent reoxidations) simplify the microstructure to a continuum, where stresses and strains are one-dimensional [26].

In that context, the aim of this work is to provide more realistic numerical microstructures that better reflect electrode processing. In particular, the sintering process should be explicitly taken into account to better reflect the complexity of the resulting microstructure. Using the discrete element method, which enforces force equilibrium for each particle in the packing during sintering, we show that indeed it is possible to reproduce complex microstructures with pore formers and/or multi-layers.

In typical SOFC/SOEC's, O_2 electrodes are bilayers usually made of yttria-stabilized zirconia (YSZ) and perovskite-type oxide like $La_{1-x}Sr_xMnO_3$ (LSM). For state-of-the-art H_2 electrodes, composites like Ni/YSZ or Ni/cerium-gadolinium oxide (CGO) cermets are popular candidates. The simulation method is thus applied here to typical LSM/YSZ and NiO/YSZ (before reduction to Ni) composite electrodes. In any case, the simulation method is general enough to be applied to other materials. For example, although CGO particles have mixed conducting properties, they may be handled by the same method since they should sinter similarly to YSZ and they have very similar elastic properties [27].

The paper is organized as follows: In Section 2, we present the particle packings that are used for generating electrodes with pore formers and/or layers. Sintering of the powder packings is described in Section 3. The reduction of NiO into Ni is simulated in Section 4 while the microstructural characteristics of the numerical microstructures are described and commented in Section 5. Whenever possible, we attempt to compare our results with experimental data from the literature.

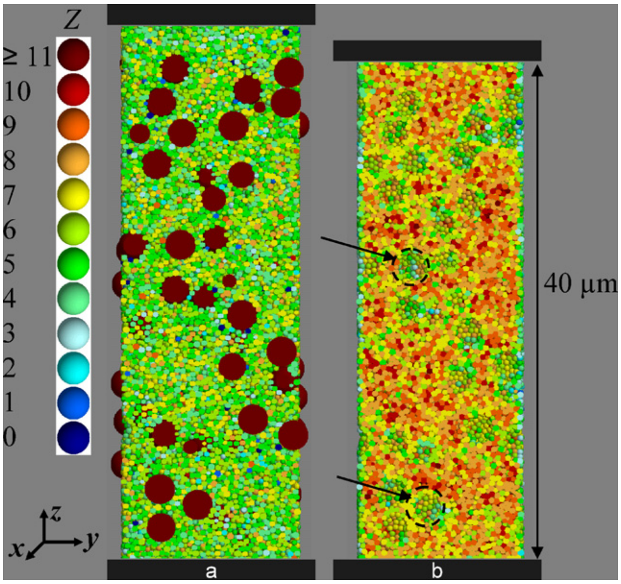

Fig. 1. Section of a NiO/YSZ-pf (with pore formers) electrode; (a) before sintering and; (b) after sintering. Pore formers are removed before sintering. Colors indicate the number of contacts *Z* for each particle. (For interpretation of the references to color in this figure legend, the reader is referred to the web version of the article.)

2. Porous electrodes generation

Typical H_2 and O_2 electrodes used in the SOEC/SOFC technologies [5] have been considered in this work. It should be noted that porous electrodes can be fabricated by different routes (tape casting, screen printing, ...) depending on the experience of the manufacturers and the final purpose of the electrodes. However, it is out of the scope of this paper to detail each step of such processes. Instead, we only considered, for the sake of simplicity, that electrodes are deposited in a green state and then consolidated by sintering to obtain their final microstructure. According to our own experience, typical green electrodes are basically constituted by a loose packing of active materials particles (NiO, YSZ, LSM) and of pore formers whom characteristics (size and volume fraction) are summarized in Table 1. Any additional precursors of these microstructures are not taken into account in this study.

Rectangular green electrodes were generated numerically by using the procedure summarized in Fig. 1 and described hereafter. A packing of spherical particles located at random positions is first generated with the constraint that particles should not contact each other. This initial packing is in a simulation box bounded by rigid planes in the *z* direction and by periodic conditions in the *x* and *y* directions. At this initial stage, particle size distribution and volume fractions of each type of particle are defined depending on the final purpose of the electrode. The particle packing is then densified with stiff elastic interactions between particles to obtain a dense green body. The procedure to generate such packings of particles has been explained in previous works [28–30]. Fig. 1a shows the green microstructure at this stage.

The first type of H_2-electrode, denoted as NiO/YSZ is obtained from a mixture of NiO and YSZ particles of the same size (0.5 μm ±5%). By default, the volume percentage of NiO in the mixture is 65%. The second type of H_2-electrode, made of the same NiO/YSZ mixture as for the first electrode, contains additionally

Table 1
Electrode characteristics. pf indicates electrodes with pore formers. The LSM/YSZ-pf electrode is a bilayer made of a YSZ + LSM layer and of a LSM layer. Two volume percentage of NiO have been studied for the NiO/YSZ and NiO/YSZ-pf electrodes.

	NiO/YSZ	NiO/YSZ-pf	LSM/YSZ-pf
Particle size (±5%)	NiO→0.5 µm YSZ→0.5 µm	NiO→0.5 µm YSZ→0.5 µm	LSM→1 µm YSZ→0.5 µm
Volume fraction	65% NiO and 35% NiO	65% NiO and 35% NiO	YSZ + LSM→50% YSZ LSM→0% YSZ
Pore former volume fraction		32%	YSZ + LSM→32% LSM→30%
Pore former size (±5%)		2 µm	YSZ + LSM→1.4 µm LSM→2.4 µm
Sintered electrode height	30 µm	40 µm	YSZ + LSM→30 µm LSM→23 µm
Number of particles	10,000	73,000	92,000

fugitive pore formers (2 µm ± 5%). It is denoted as NiO/YSZ-pf. Once pore formers are removed from this second electrode, the volume percentage is 65% volume of NiO as for the first electrode. Note that the electrode is not graded and that the active zone is assumed to spread all along the thickness. The microstructure of this H_2-electrode is illustrated in Fig. 1b before the reduction step. The partially sintered microstructure exhibits two populations of pores: the small pores left in between partially sintered particles, and the large pores originating from the removal of the pore formers. This double porosity compares qualitatively well with the anodes sintered with fugitive pore formers by Suzuki et al. [5]. These anodes were made of NiO-Sc-stabilized zirconia and Ce-doped zirconia. The double porosity is linked to the relatively low temperature used by these authors (1250 °C), which ensures only partial sintering of the particles, and is clearly observed in their Fig. 2 for cell A.

The third electrode is a O_2 electrode made of two layers which are subsequently co-sintered together. The active layer, adjacent to the electrolyte, is a mixture of YSZ (0.5 µm ± 5%) and of LSM (1 µm ± 5%) particles and of pore formers (1.4 µm ±5%), while the diffusion layer is made of LSM particles (1 µm ±5%) with 2.4 µm ± 5% fugitive pore formers. This electrode is denoted as LSM/YSZ-pf. These electrodes are typical of composite electrodes encountered in the literature [5]. A typical microstructure of such a bilayered electrode observed after the sintering stage on commercial cells is illustrated in Fig. 2. The narrow size distribution that we have used is obviously an oversimplification of real microstructures. Literature provides examples of porous electrodes with a rather uniform size distribution [3–5,7] (and also Fig. 2 in this work) and examples where the size distribution is much larger [8,9,13]. For sake of simplicity, we have chosen to leave the issue of large particle size distribution for future work.

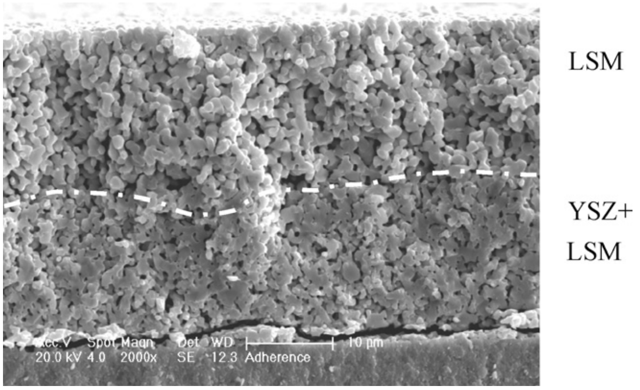

Fig. 2. Microstructure of the LSM/YSZ bilayer. The white dotted curve indicates the interface between the composite layer YSZ + LSM and the homogeneous LSM layer. YSZ and LSM cannot be distinguished in this SEM micrograph.

Fig. 1a shows the microstructure of the NiO/YSZ-pf packing before sintering. The large pore former particles are packed together with the other particles. Colors indicate the coordination number (number of contacts with other particles) for each individual particle. The coordination number is a good indicator of the local packing density. For electrodes containing pore formers such as the electrode depicted in Fig. 1, pore former particles are eliminated before the numerical sintering. This is to mimic real ceramic processes in which fugitive polymer pore formers are introduced and then burned out at high temperature [5,8,9]. All packings have $\varepsilon_0 = 0.5$ initial porosity after fugitive pore former removal, prior to sintering.

Electrode heights are typical of electrolyte-supported cells (30 to 40 µm). Also, it should be noted that in order to keep reasonable CPU time for the simulation, it is not possible to consider the whole width of the electrode in the *x* and *y* directions. Instead, we simulate a pillar which is typically 15 to 20 µm wide. Still, the number of simulated particles (10,000 for the NiO/YSZ electrode without pore former and >70,000 for the electrodes with pore formers) should be large enough to ensure that the numerical microstructure constitutes a representative volume element of the electrode.

3. Sintering

All packings are subjected to a numerical sintering procedure which has been detailed elsewhere [30–32]. Briefly, it consists in introducing contact forces that account for sintering phenomena between particles at high temperature. Bouvard and McMeeking's model, which considers grain boundary and surface diffusion to be the main mechanisms of mass transport, is used [33]. We denote γ_s as the surface energy and Δ_b as the diffusion parameter:

$$\Delta_b = \frac{\Omega}{kT}\delta_b D_b, \tag{1}$$

where $D_b = D_{0b}\exp(-Q_b/RT)$ is the diffusion coefficient for vacancy transport in the grain boundary with thickness δ_b and activation energy Q_b and Ω is the atomic volume. For two spherical particles of radii R_1 and R_2, having a contact radius a_b and indentation h_b (Fig. 3), the normal force N_s acting on the contact is given by:

$$N_s = \frac{\pi a_b^4}{8\Delta_b}\frac{\mathrm{d}h_b}{\mathrm{d}t} - \frac{9}{4}\pi R^* \gamma_s, \tag{2}$$

where $R^* = R_1R_2/(R_1 + R_2)$. The normal contact force in Eq. (2) is the sum of two terms. The first term is a normal viscosity term, which acts both in tension or compression depending on the rate of approach of the two particles ($\mathrm{d}h_b/\mathrm{d}t$). The second term, linked to surface energy, acts only in tension and is independent of contact size.

Similarly, a tangential contact force T_s opposes the tangential component of the relative velocity at the contact, $\mathrm{d}u/\mathrm{d}t$, and is given

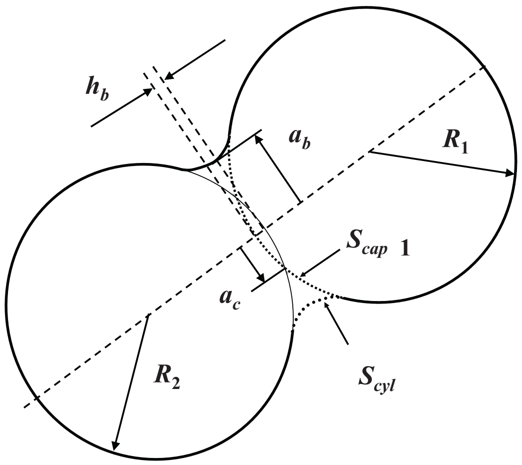

Fig. 3. Schematic of two particles forming a sintered bond of radius a_b. The S_{cap1} surface is subtracted to the particle surface while S_{cyl} is added to compute the total free surface in Eq. (6).

by [34,35]:

$$T_s = -\eta \frac{\pi a_b^2 R^{*2}}{2\Delta_b} \frac{\mathrm{d}u}{\mathrm{d}t}, \tag{3}$$

where η is a viscous parameter with no dimension. In the simulations, $\eta = 10^{-3}$ for contacts between particles and $\eta = 0$ for contacts between particles and the substrates [32]. We assume that contacts become rapidly large enough to oppose any rotation of the particles.

For sintering, free surfaces along the x and y directions are used and replace the periodic conditions previously used for compaction. The two rigid planes with normal along the z direction are maintained during sintering and thus act as planar substrates. Particles form sintered bonds both with neighboring particles and with the two substrates. The bond size a_b between two particles of radii R_1 and R_2 grows according to Coble's model [36]:

$$\frac{\mathrm{d}a_b}{\mathrm{d}t} = 2\frac{R^*}{a_b}\frac{\mathrm{d}h_b}{\mathrm{d}t}, \tag{4}$$

which is in good accordance with various numerical simulations on pairs of particles of equal size [33] or different sizes [37]. When integrating Eq. (4) from an initial value $a_b = 0$, it yields a bond radius $a_b^2 = 4R^*h_b$ which is larger (by a $\sqrt{2}$ factor) than the contact radius obtained from a simple geometric intersect of two overlapping spheres (a_c). This is because Coble's model accounts for volume conservation as sintering proceeds. This larger contact size impacts on the calculation of the Triple Phase Boundary length and is neglected by models that approximate sintering to the growth of particle radii [17,20,21,24,25].

As shown by Fig. 3, sintering results in particle centers approaching each other and thus particles becoming truncated spheres. In other words, densification of the powder proceeds in the discrete element simulations by the gradual overlap of particles. This is accompanied also by the appearance of new contacts between particles. This is clearly demonstrated by comparing Fig. 1a and Fig. 1b, which also shows a decrease of the height of the particulate assembly.

There is a lack of data corresponding to the sintering material parameters relevant for SOFC manufacturing. Thus, we do not have access to the sintering material parameters that are needed in Eqs (1), (2) and (3) for each type of ceramic particle modeled here (NiO, YSZ and LSM). To tackle this problem, we make the assumption that all particles of a given size sinter with the same kinetics, irrespective of their composition. Under this assumption and recognizing that the exact kinetics of densification of the porous microstructure (the time necessary to attain a given relative density at a given temperature) is out of reach, we may obtain realistic microstructures.

This is because examination of Eq. (2) indicates that for a $\tau = R^4/(\Delta_b \gamma_s)$, where R is a length scale equal to the mean particle radius, gives a normalized time which introduces time-temperature equivalence (through the Δ_b term). The expression of τ is obtained by enforcing zero contact force (force equilibrium, $N_s = 0$) and by relating lengths (R^*, a_b and h_b) to the mean radius R. This normalized time correctly reveals that large particles sinter slower, and that larger temperature are associated with shorter sintering time. Using this normalized time in our simulation, we may use an arbitrary set of material parameters. Here, we have used alumina parameters ($D_{0b} = 1.310^{-08}$ m^3 s^{-1}, $\Omega = 8.4710^{-30}$ m^3, $Q_b = 475$ kJ mole^{-1}, and $\gamma_s = 1.1$ J m^{-2}) [38,39]. Thus, while the physical time necessary to reach a given microstructure is dependent on this set of material parameters (and on the sintering temperature), the microstructure itself is independent of the material parameters in our model.

However, differences in particle size in the packing play an important role in the sintering model through the R^* effective radius. In particular, Eqs. (2) and (4) show that the time necessary to decrease porosity to a given value in a volume element made of particles of size R scales with R^{-4} [37,40]. Thus, when force equilibrium is ensured, the rate of approach ($\mathrm{d}h_b/\mathrm{d}t$) between two YSZ particles (0.5 μm size) or between a YSZ particle and an LSM particle (1 μm size) is larger than between two LSM particles.

Note also that for simplicity we have not considered coarsening between particles during sintering as in a previous work [31]. This is a reasonable assumption for the partial sintering process which we are modeling here.

The sintering procedure presented above has been applied to the three electrodes described in Table 1. Starting from an initial porosity of $\varepsilon_0 = 0.5$, sintering was interrupted at decreasing amounts of porosity to study the evolution of the main microstructural features which are pertinent to electrochemical processes (see Section 5).

Concerning the cosintering of the bilayered LSM/YSZ-pf electrode, Fig. 4 shows the evolution of the local porosity ε along the z axis at various sintering times. The two layers have started from the same approximate initial porosity ($\varepsilon_0 \approx 0.5$). The initial porosity exhibits some deviation from the 0.5 mean value due to the finite size of the simulated volume. Also, the initial interface between the LSM layer and the LSM + YSZ layer exhibits a smaller porosity. This is due to the fact that by construction of the bilayer, no large pore can cross the interface. Recall that large pores are initially introduced in the packing as pore former particles (see Fig. 1).

Note how this denser initial interface has translated from 32 μm height to 27 μm height and has kept its relatively lower porosity as sintering proceeded. More importantly, because the YSZ particles are smaller (0.5 μm) than the LSM particles (1 μm), the YSZ–LSM layer sinters faster than the LSM layer. The larger densification of the YSZ–LSM layer is observable from the surface distortion at the interface with the LSM layer that constrains somewhat the bottom layer. Recall that the bilayer exhibits free surfaces in the x and y directions during the sintering stage. At a mesoscopic length scale, curve b in Fig. 4 clearly indicates that the porosity of the YSZ–LSM layer becomes much smaller ($\varepsilon \approx 0.18$) than the porosity of the LSM layer ($\varepsilon \approx 0.35$) as sintering proceeds.

This is an encouraging indication that our sintering model is behaving correctly. Indeed, we have observed on experimentally cosintered bilayered LSM/YSZ electrodes (Fig. 2) with initial microstructures characterized by the properties given in Table 1 that the average porosity of the LSM and of the YSZ–LSM layers are 0.34 and 0.18, respectively. These numbers compare favorably with curve b in Fig. 4. Again, it should be clear that the exact heating cycle (time and temperature) necessary to obtain the microstructure defined by curve b cannot be reproduced by our model because

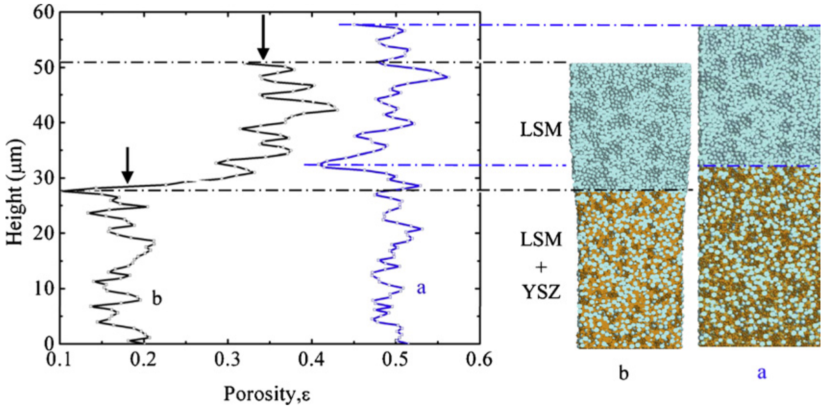

Fig. 4. Evolution of the porosity along the z axis of the LSM/YSZ-pf electrode (a) before sintering and (b) after sintering. The corresponding final bilayered microstructure is shown on the right hand side. Arrows indicate the experimentally measured average porosity for each layer.

it would necessitate the knowledge of diffusion coefficients and surface energies which are not available for YSZ and LSM. Still, if the sintering simulation is stopped when the porosity of the YSZ–LSM layer is approximately 0.18, the model appropriately predicts that the LSM layer porosity, which contains larger particles, is approximately 0.35.

4. Reduction of NiO → Ni

Once sintered, the NiO ceramic particles in the anode are reduced to Ni metal on exposure to hydrogen. The reduction of the NiO particles has been numerically simulated by a simple procedure based on the model proposed by Klemensø et al. [41]. The YSZ particles are bonded together with stiff elastic bonds (Young's modulus 220 GPa) and infinite strength. The NiO particles are bonded together and to YSZ particles by weaker bonds that may deform easily if strained (Young's modulus 2 GPa). This is to model the fact that the NiO ceramic particles become softer metallic particles at high temperature during reduction. Still, it should be clear that we do not attempt to model the plastic (or viscoplastic) deformation that Ni particles may undergo at high temperature. The NiO particles are then submitted to a gradual diameter reduction to account for the NiO → Ni phase change. We have chosen to look at two values for the volume reduction of the nickel phase: 25% and 41%, corresponding to 9% and 16% radius reduction, respectively. The value of 25% may be regarded as typical of the amount of a partial reduction [41–43], while the 41% is the upper theoretical limit for the full reduction of NiO to Ni [44]. The size reduction implies a reorganization of the Ni and YSZ particles which is accounted for in the discrete simulations by imposing force equilibrium to each particle. Note that, contrarily to the sintering stage, the sample is not bound to any substrate in the reduction stage.

Two NiO volume fractions ($\Phi_{\mathrm{NiO}} = 35\%$ and $\Phi_{\mathrm{NiO}} = 65\%$) were simulated to study the effect of mechanical percolation of the YSZ phase. By mechanical percolation we mean that a rigid skeleton of YSZ particles that can sustain forces without large deformation has formed. Such percolation is always larger than the more classical geometrical percolation threshold [45]. When the YSZ volume fraction is only 35% ($\Phi_{\mathrm{NiO}} = 65\%$), mechanical percolation is not enforced. This has some important effect on the porosity increase that should be brought by NiO reduction. On the contrary, when the YSZ volume fraction is 65% ($\Phi_{\mathrm{NiO}} = 35\%$), mechanical percolation is ensured. In that case, owing to the large rigidity of the YSZ–YSZ bonds, a YSZ skeleton is formed and it is mostly the Ni particles that rearrange during reduction.

If the YSZ phase percolates mechanically, it may be assumed that no macroscopic shrinkage will occur upon reduction since a YSZ skeleton holds the sample. In that case, the porosity ε may be simply deduced from the following equation:

$$\varepsilon = \varepsilon_i + \Delta V_{\mathrm{Nio}\to\mathrm{Ni}}(1-\varepsilon_i)\Phi_{\mathrm{NiO}}, \tag{5}$$

where ε_i is the porosity before reduction and $\Delta V_{\mathrm{Nio}\to\mathrm{Ni}}$ is the volume reduction of the Ni phase (from 0 to 0.41). Fig. 5a and b shows the evolution of porosity as reduction proceeds ($\Delta V_{\mathrm{Nio}\to\mathrm{Ni}} = 0$ to 41%) for samples with and without pore formers, respectively. They indicate that indeed, when mechanical percolation is enforced ($\Phi_{\mathrm{NiO}} = 35\%$), Eq. (5) is in good accordance with simulations. This is consistent with experimental data that report very little macroscopic shrinkage upon the first reduction for materials which contain a sufficient amount of YSZ phase [41,46,47].

However, when the NiO volume fraction is high ($\Phi_{\mathrm{NiO}} = 65\%$), the porosity increase given by Eq. (5) overestimates the porosity increase calculated from the simulations. This is because, in that case, the sample experience macroscopic shrinkage. Experimental data confirms that in certain cases, macroscopic shrinkage may occur, thus limiting the porosity increase of the sample [46,48]. It has also been reported that significant shrinkage may occur when the volume fraction of YSZ is small ($\Phi_{\mathrm{NiO}} = 90\%$) [48]. This is in good accordance with the present simulations which demonstrate the importance of the formation of a YSZ skeleton upon reduction.

The curves shown in Fig. 5a and b are reported for an initial porosity (ε_i, porosity before reduction) of approximately 30%. The same qualitative behavior was observed for the other initial porosities.

In accordance with the porosity evolution reported above, we have observed different reduced microstructures, depending on the initial YSZ volume fraction (35% or 65%). If the YSZ volume fraction is large (65%), the resulting microstructure accommodates the volume change predominantly by pore opening inside the YSZ skeleton while macroscopic volume change does not occur. If the volume fraction is small (35%), shrinkage partially accommodates the volume change of Ni particles.

Note that by the end of the simulated reduction procedure the cermet is in the immediate reduced state as opposed to the long-term reduced state which would involve coarsening of the Ni particles [41]. Ni coarsening is not included in the model in its present state.

5. Microstructural characterization

Once sintered, the numerical microstructures may be characterized to obtain some useful information on microstructural parameters that are critical for electrochemical efficiency. We have focused on two parameters: the pore surface area which affects

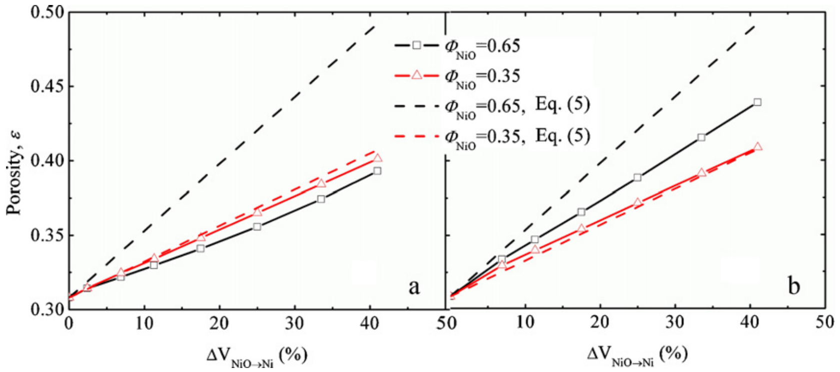

Fig. 5. Evolution of the macroscopic porosity of samples without pore former (a) and with pore formers (b) upon reduction for two initial volume fractions of NiO (Φ_{NiO} = 35 and 65%). Broken lines indicate the evolution of porosity when no macroscopic shrinkage occurs (Eq. (5)).

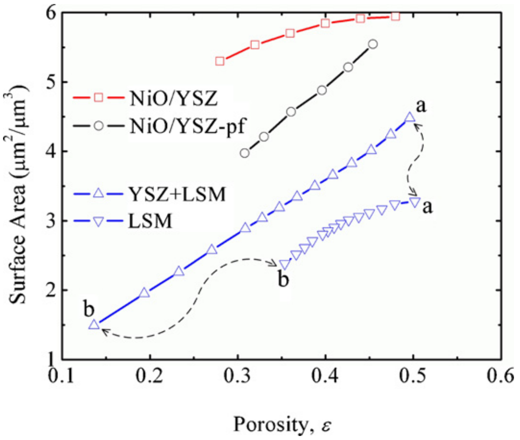

Fig. 6. Evolution of the pore surface per unit volume versus the macroscopic porosity ε of NiO–YSZ electrodes with and without pore former before reduction and of bilayered electrode LSM/YSZ-pf. The arrowed lines connect the LSM and the YSZ + LSM layers for the initial (a) and final (b) microstructures as shown in Fig. 4.

adsorption and surface diffusion, and the total length of Triple Phase Boundaries (L_{TPB}) where electrolyte, electrocatalyst and gas phase react. The reaction rate of the three phases is believed to be correlated to the TPB length.

5.1. Pore surface area per unit volume of sample

The pore surface area (free surface) per unit volume, is calculated from the partially sintered assembly of *N* spherical particles by considering their surface and the surface geometry of each of the *K* contacts in the electrode (Fig. 3):

$$S = \frac{(1-\varepsilon)\left(\sum_{i=1}^{N}4\pi R_i^2 - \sum_{k=1}^{K}\left(S_{k,cap1}+S_{k,cap2}\right)+\sum_{k=1}^{K}S_{k,cyl}\right)}{\left(\sum_{i=1}^{N}(4/3)\pi R_i^3\right)}, \tag{6}$$

where $S_{k,cap1} + S_{k,cap2}$ is the total surface of the two caps at the intersection of the two particles and $S_{k,cyl}$ is the surface of the bonding between the two particles (approximated by a cylinder). Note that the sum is made on all particle free surfaces for a given electrode, irrespective of their nature (NiO, Ni, YSZ, or LSM).

Fig. 6 shows the evolution of the pore surface area per unit volume as a function of the porosity ε attained during sintering for the NiO/YSZ electrode before reduction, without pore former (NiO/YSZ) and with pore former (NiO/YSZ-pf). Quite predictably, the pore surface area decreases as porosity ε decreases. More interestingly, Fig. 6 indicates that for a given macroscopic porosity, introducing pore formers leads to a decrease of the total free surface. This is because there are two populations of pores induced by the microstructure with pore formers: the natural small pores left in between particles, and the large pores that are left after the removal of fugitive pore formers. When considering the total pore surface *per unit volume* for a given macroscopic porosity, the simulations indicate that it is more beneficial to use small pores than large ones. However, large percolating pores will certainly have an overall beneficial effect when electrode performance is limited by gas diffusion.

The same analysis is carried out on the LSM/YSZ + LSM bilayer. In that case, we distinguish the two layers LSM and YSZ + LSM in Fig. 6. Because the LSM particles are double the size of the NiO or YSZ particles, the free surfaces *per unit volume* of the LSM and YSZ + LSM layers are smaller. More generally, it may be shown that for a given microstructure, *S* is approximately inversely proportional to the average particle size. Thus, the results of Fig. 6 may easily be generalized to other particle sizes. Also, for a monomodal powder made of particles of size 2*R*, *S* is bounded by:

$$S_{\max} = \frac{6(1-\varepsilon)}{2R}, \tag{7}$$

when contacts between particles are small. Taking into account this particle size effect, we note that our results agree with the experimental data of Song et al. [7] on LSM-YSZ composites sintered at three different temperatures which lead to various final particle sizes. These authors, using line intercept method to analyze digital images of their microstructures, have measured free surface per unit volume of 5, 7 and 10 $\mu m^2\ \mu m^{-3}$ for 1 μm, 600 nm and 400 nm approximate particle size, respectively (their Fig. 3).

Fig. 7 shows the effect of reducing NiO to Ni on the free surface for Φ_{NiO} = 65%. In accordance with the porosity increase due to reduction, Fig. 7 indicates that pore surface increases as Ni reduction progresses. Inspection of Eq. (6) shows that the total pore surface is the sum of a term that will decrease with reduction (surface of Ni particles) and of a term which will increase as contacts between Ni and between Ni and YSZ particles disappear (the cap surface of the contacts). The third term in Eq. (6) can be neglected in most conditions. Thus, it is not surprising that the overall increase in free surface is limited during reduction and that its evolution is not monotonic. For Φ_{NiO} = 35%, we observed similar results to those shown in Fig. 7, indicating that YSZ percolation does not play a dominant role in the evolution of *S*.

Pore surfaces were measured experimentally in the literature for Ni-YSZ cermets by scanning electron microscope [44,49] and nondestructive tomographic imaging technique [50]. The total free surface reported in these works are 2.4 $\mu m\ \mu m^{-2}$[44,49] and 6.8 $\mu m\ \mu m^{-2}$[50] for particle sizes that are somewhat larger than

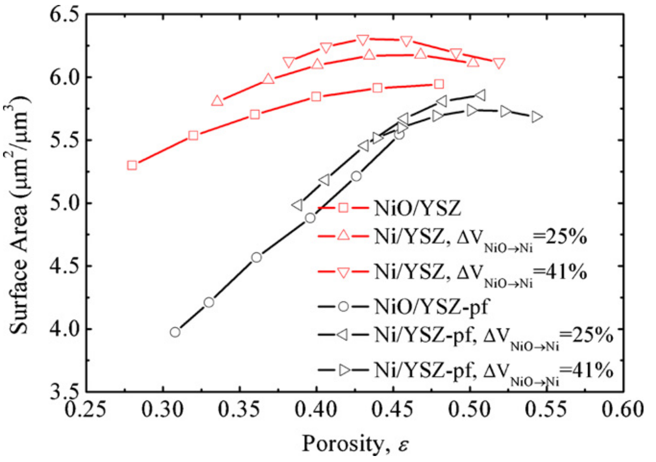

Fig. 7. Effect of NiO reduction on the NiO/YSZ and NiO/YSZ-pf electrodes for $\Phi_{NiO} = 65\%$.

those used in our simulations. Again, these numbers are consistent with the results shown in Fig. 7 and with Eq. (7).

5.2. Triple Phase Boundary Length

The total length of TPB per unit volume, L_{TPB}, has been calculated similarly to the pore surface by considering each contact between LSM and YSZ particles or between Ni and YSZ particles. For completeness, we have also calculated a TPB length between NiO and YSZ particles to study the effect of reduction on the geometry of bonded contacts between NiO and YSZ particles. L_{TPB} is calculated by summing the perimeters $2\pi a_b$ for those contacts (Fig. 3).

Fig. 8 shows the evolution of L_{TPB} with macroscopic porosity ε for non-reduced NiO/YSZ electrodes and for YSZ/LSM electrodes. Since the average number of bonds and the average bond size a_b increase as sintering progresses, L_{TPB} increases with decreasing porosity. However, contrarily to Fig. 6, Fig. 8 indicates that it is advantageous to introduce pore formers to increase L_{TPB}. For a total given macroscopic porosity ε, the introduction of pore formers allows a 60–70% increase in L_{TPB}. Although verified only for the NiO/YSZ electrode, this result is likely to remain valid for any type of porous electrode. This is because for a given macroscopic porosity, the introduction of large pore formers imposes a denser packing of the remaining particles, thus increasing the average bond size a_b and the resulting L_{TPB} [30].

Caution should be taken in ascribing too much a positive role to pore formers on the increase of performance of the porous electrode. As shown in Fig. 1, there are two populations of pores in microstructures with pore formers: the natural small pores left in between particles, and the large pores that are left after the removal of fugitive pore formers. The zones in between large pores, which contain many TPB points brought by enhanced packing, must still be able to diffuse gases in order to obtain good overall electrochemical performances and thus cannot be too dense.

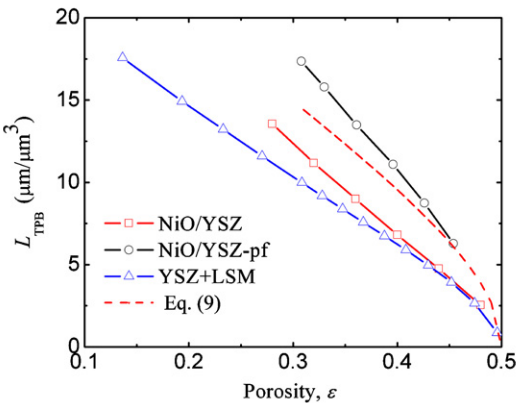

Fig. 8. Evolution of L_{TPB} with porosity for non-reduced NiO/YSZ electrodes and for the YSZ + LSM layer of the LSM/YSZ-pf electrode.

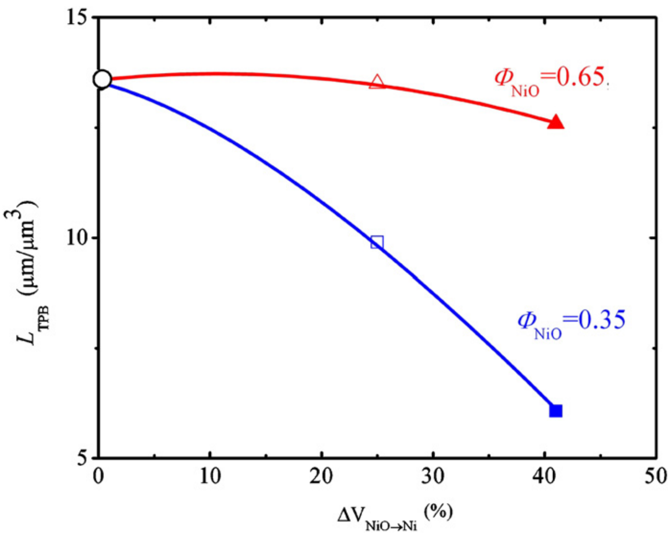

Fig. 9. Evolution of L_{TPB} upon reduction for NiO/YSZ without pore former and initial porosity $\varepsilon_i = 0.27$ for two volume fractions of NiO.

The lowest values of L_{TPB} are found in Fig. 8 for the YSZ + LSM layer. This is due to the already mentioned fact that LSM particles are larger (1 μm) than NiO and YSZ particles (500 nm). As for the free surface calculated in the preceding section, the calculated L_{TPB} should be considered as a lower bond since we consider spherical particles as opposed to more realistic non-spherical particles. Conversely, polydispersity (as opposed to our narrow size distribution) should decrease the value of L_{TPB} as shown by Kenney et al. [21] who have calculated that realistic size distribution may lead to a decrease of L_{TPB} by as much as 40%.

The effect of reduction of NiO on L_{TPB} is shown in Fig. 9 for the case of an electrode without pore former and an initial porosity $\varepsilon_i = 0.27$. When the volume fraction of NiO is small ($\Phi_{NiO} = 0.35$), a rigid skeleton of YSZ particles is formed as described in Section 4. The consequence is that volume reduction of NiO to Ni is accommodated predominantly by pore opening in the YSZ skeleton and by contact losses without macroscopic shrinkage. The consequence is a decrease of the overall L_{TPB} as shown in Fig. 9. On the contrary, when no rigid YSZ skeleton is formed ($\Phi_{NiO} = 0.65$), volume reduction is accommodated by macroscopic shrinkage and we have actually observed that in that case, new contacts between Ni and YSZ particles may actually be brought by reduction. In that case, the decrease in L_{TPB} is much less.

All electrodes, with or without pore formers, exhibit the same general trend described in Fig. 9. This is shown in Fig. 10a and b, where the variations in L_{TPB} for various initial porosities is collected. The figure indicates that the increase in porosity is coupled with a large decrease in L_{TPB} for samples with a rigid YSZ skeleton. Also, it may be noticed that the gain in L_{TPB} brought by the use of pore formers is preserved upon reduction for a given relative density. Thus, it may be concluded that pore formers should have beneficial effect on L_{TPB} even when accounting for the reduction stage.

When no pore former is present and all particles are of the same size $2R$, we have proposed a simple approximation for L_{TPB} as a function of the composition of the composite in one of the particle

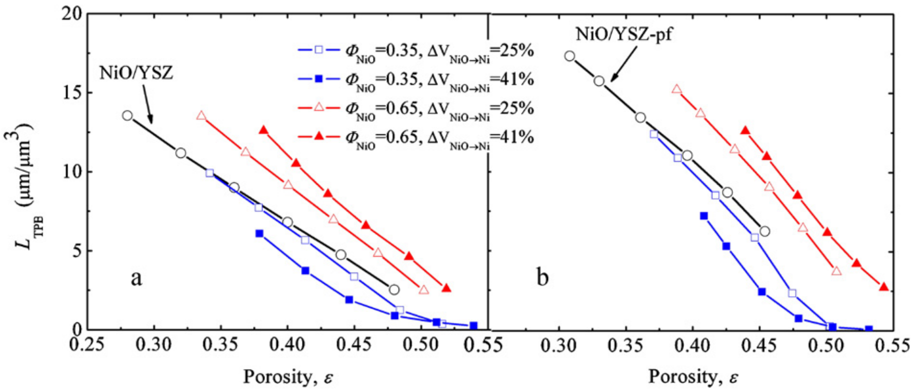

Fig. 10. Evolution of L_{TPB} with porosity upon reduction for NiO/YSZ without pore former (a) and with pore former (b). The effect of the volume fraction of NiO, Φ_{NiO}, is demonstrated for both types of electrodes.

type, Φ [18]:

$$L_{TPB} = \frac{3(1-\varepsilon)Z}{R^2}\Phi(1-\Phi)\sqrt{1-\left(\frac{1-\varepsilon_0}{1-\varepsilon}\right)^{1/3}}, \tag{8}$$

where Z is the average contact number per particle and ε_0 is the initial porosity of the particle packing, before sintering. The exact value of ε_0 is difficult to ascertain. However, for the isotropic sintering of a layer which shrinks from an initial thickness t_0 to a final thickness t, the term $\left((1-\varepsilon_0)/(1-\varepsilon)\right)^{1/3}$ may be estimated as t/t_0. Approximating Z by 6, a simpler and more useful version of Eq. (8) can thus be written:

$$L_{TPB} = \frac{72(1-\varepsilon)}{d^2}\Phi(1-\Phi)\sqrt{1-\frac{t}{t_0}}, \tag{9}$$

where d is the particle size. Eq. (9) only introduces material and process parameters that should be accessible to experimentalists.

Eq. (9) may be compared to the L_{TPB} value of the monomodal NiO/YSZ powder sintered numerically. Fig. 8 shows that, although it overestimates L_{TPB} as compared to the more realistic numerical simulations, it is still a satisfactory approximation. The overestimation comes from the approximation, used in deriving Eq. (9), that particles do not rearrange during sintering (also called the affine assumption). This leads to an overestimation of a_b and thus to an overestimation of L_{TPB}.

Eq. (9) shows that decreasing the particle size is the most efficient way to increase TPB length per unit volume. In reality, this may be achieved, for a given initial powder size, by decreasing the sintering temperature to avoid coarsening [4]. Furthermore, for a given particle size, increasing contact number and decreasing porosity also allows larger L_{TPB} to be obtained. The $\Phi(1-\Phi)$ term in Eq. (9) indicates that having a mixture close to 50–50% composition of ionic and electronic conducting particles is beneficial for L_{TPB} (although this does not ensure good overall conductive properties due to percolation effects as demonstrated in [22]).

Another useful feature of Eq. (9) is that it explains quite simply the large scatter of L_{TPB} values found in the literature. For Ni-YSZ anodes quantified by coupling focused ion beam and scanning electron microscopy (FIB-SEM), L_{TPB} values have been reported by three different teams. Iwai et al. found $L_{TPB} = 2.6\,\mu\text{m}\,\mu\text{m}^{-3}$ at 50% porosity and for ~3 μm (Ni) and ~2 μm (YSZ) particles [51]. Wilson et al. reported $L_{TPB} = 4.3\,\mu\text{m}\,\mu\text{m}^{-3}$ for ~2 μm Ni and ~1 μm YSZ particles and 20% porosity [44]. Shearing et al. obtained $10\,\mu\text{m}\,\mu\text{m}^{-3}$ to $13\,\mu\text{m}\,\mu\text{m}^{-3}$ for approximately 1.5 μm Ni and YSZ particles and 10% porosity [52,53]. The above reported values of L_{TPB} are consistent with each other when considering the approximate proportionality rule derived from Eq. (9):

$$L_{TPB} \propto \frac{(1-\varepsilon)}{R^2}, \tag{10}$$

Thus, we conclude that the large scatter found in the literature on L_{TPB} values is mainly due to porosity and particle size differences between the samples.

6. Conclusions

Numerical microstructures representing partially sintered porous electrodes have been generated using discrete simulations. The originality of the present approach is to include the sintering process in the simulation to allow for realistic microstructures to be generated. We believe, in particular, that the bilayered structures and the structures incorporating pore formers that have been numerically generated here and which are now routinely encountered in real electrodes, offer an interesting tool for studying important microstructural characteristics.

It has been shown that the introduction of pore formers has mainly a positive effect on the microstructure of the electrode. This is because, although it reduces slightly the surface area in the electrode, large pores brought by pore formers provide an easy path for species diffusion and increase the TPB length in the electrode.

The present results also show the importance of the NiO volume fraction upon reduction of NiO–YSZ composites. When the YSZ particles are forming a rigid skeleton, reduction leads to a large increase in porosity and a decrease in the TPB length. When the NiO volume fraction is large enough to prevent the formation of a YSZ skeleton, macroscopic porosity does not increase as much. Instead, macroscopic shrinkage is observed.

Some oversimplifications in our model and in the numerical microstructures should be addressed. Although, our sintering model correctly takes particle size into account, it assumes that all particles of a given size, irrespective of their material (NiO, YSZ, LSM) sinter with the same kinetics. This simplification could be addressed by empirically comparing real electrode microstructures with those generated numerically and modifying sintering parameters (typically the surface energy, γ_s) for each type of contact to approach the real microstructure. Also, the narrow particle size distribution assumed here is clearly an oversimplification that should be addressed. The discrete element method is a very effective tool for simulating size distribution effects in powders [55,54]. This is certainly an avenue for simulating even more realistic porous electrodes.

Finally, the present numerical microstructures may be further used for mechanical treatment to obtain the elastic and fracture properties of porous electrodes. In particular, they will be useful to quantify the effect of large pores or to evaluate the effect of NiO reduction on the mechanical properties of the electrodes. This work is presently in progress.

Acknowledgements

The ANR PanH is greatly acknowledged for financial support (project MOISE).

References

[1] M.J.L. Østergård, C. Clausen, C. Bagger, M. Mogensen, Electrochim. Acta 40 (1995) 1971–1981.

[2] S.M. Haile, Acta Mater. 51 (2003) 5981–6000.

[3] F. Tietz, H.-P. Buchkremer, D. Stover, J. Electroceram. 17 (2006) 701–707.

[4] J.R. Smith, A. Chen, D. Gostovic, D. Hickey, D. Kundinger, K.L. Duncan, R.T. DeHoff, K.S. Jones, E.D. Wachsman, Solid State Ionics 180 (2009) 90–98.

[5] T. Suzuki, Z. Hasan, Y. Funahashi, T. Yamaguchi, Y. Fujishiro, M. Awano, Science 325 (2009) 852–855.

[6] J.M. Vohs, R.J. Gorte, Adv. Mater. 21 (2009) 943–956.

[7] H.S. Song, W.H. Kim, S.H. Hyun, J. Moon, J. Electroceram. 17 (2006) 759–764.

[8] M. Prestat, A. Morandi, A. Heel, L. Holzer, P. Holtappels, T.J. Graule, Electrochem. Commun. 12 (2010) 292–295.

[9] M. Boaro, J.M. Vohs, R.J. Gorte, J. Am. Ceram. Soc. 86 (2003) 395–400.

[10] M.L. Fontaine, C. Laberty-Robert, F. Ansart, P. Tailhades, J. Power Sources 156 (2006) 33–38.

[11] P. Holtappels, C. Sorof, M.C. Verbraeken, S. Rambert, U. Vogt, Fuel Cells 6 (2006) 113–116.

[12] J. Hu, Z. Lu, K. Chen, X. Huang, N. Ai, X. Du, C. Fu, J. Wang, W. Su, J. Membr. Sci. 318 (2008) 445–451.

[13] J.-H. Lee, J.-W. Heo, D.-S. Lee, J. Kim, G.-H. Kim, H.-W. Lee, H.S. Song, J.-H. Moon, Solid State Ionics 158 (2003) 225–232.

[14] P. Costamagna, P. Costa, V. Antonucci, Electrochim. Acta 43 (1998) 375–394.

[15] X. Deng, A. Petric, J. Power Sources 140 (2005) 297–303.

[16] D. Chen, Z. Lin, H. Zhu, R.J. Kee, J. Power Sources 191 (2009) 240–252.

[17] A. Abbaspour, J.-L. Luo, K. Nandakumar, Electrochim. Acta 55 (2010) 3944–3950.

[18] L.C.R. Schneider, C.L. Martin, Y. Bultel, D. Bouvard, E. Siebert, Electrochim. Acta 52 (2006) 314–324.

[19] A. Ali, X. Wen, K. Nandakumar, J. Luo, K.T. Chuang, J. Power Sources 185 (2008) 961–966.

[20] J. Golbert, C.S. Adjiman, N.P. Brandon, Ind. Eng. Chem. Res. 47 (2008) 7693–7699.

[21] B. Kenney, M. Valdmanis, C. Baker, J.G. Pharoah, K. Karan, J. Power Sources 189 (2009) 1051–1059.

[22] L.C.R. Schneider, C.L. Martin, Y. Bultel, L. Dessemond, D. Bouvard, Electrochim. Acta 52 (2007) 3190–3198.

[23] S.M. Sweeney, C.L. Martin, Acta Mater. 51 (2003) 3635–3649.

[24] S. Sunde, J. Electrochem. Soc. 143 (1996) 1123–1132.

[25] S. Sunde, J. Electroceram. 5 (2000) 153–182.

[26] M.H. Pihlatie, H.L. Frandsen, A. Kaiser, M. Mogensen, J. Power Sources 195 (2010) 2677–2690.

[27] A. Selçuk, A. Atkinson, J. Eur. Ceram. Soc. 17 (1997) 1523–1532.

[28] C.L. Martin, D. Bouvard, S. Shima, J. Mech. Phys. Solids 51 (2003) 667–693.

[29] C.L. Martin, R.K. Bordia, Phys. Rev. E 77 (2008) 031307.

[30] X. Liu, C.L. Martin, G. Delette, D. Bouvard, J. Mech. Phys. Solids 58 (2010) 829–842.

[31] C.L. Martin, L.C.R. Schneider, L. Olmos, D. Bouvard, Scripta Mater. 55 (2006) 425–428.

[32] C.L. Martin, R.K. Bordia, Acta Mater. 57 (2009) 549–558.

[33] D. Bouvard, R.M. McMeeking, J. Am. Ceram. Soc. 79 (1996) 666–672.

[34] H. Riedel, H. Zipse, J. Svoboda, Acta Metall. 42 (1994) 445–452.

[35] R. Raj, M.F. Ashby, Metall. Trans. 2 (1971) 1113–1123.

[36] R.L. Coble, J. Am. Ceram. Soc. 41 (1958) 55–62.

[37] J. Pan, H. Le, S. Kucherenko, J.A. Yeomans, Acta Mater. 46 (1998) 4671–4690.

[38] W. Wonisch, O. Guillon, T. Kraft, M. Moseler, H. Riedel, J. Roedel, Acta Mater. 55 (2007) 5187–5199.

[39] B. Henrich, A. Wonisch, T. Kraft, M. Moseler, H. Riedel, Acta Mater. 55 (2007) 753–762.

[40] F. Parhami, R.M. McMeeking, A.C.F. Cocks, Z. Suo, Mech. Mater. 31 (1999) 43–61.

[41] T. Klemensø, C. Chung, P.H. Larsen, M. Mogensen, J. Electrochem. Soc. 152 (2005) A2186–A2192.

[42] M. Radovic, E. Lara-Curzio, Acta Mater. 52 (2004) 5747–5756.

[43] D. Waldbillig, A. Wood, D.G. Ivey, Solid State Ionics 176 (2005) 847–859.

[44] J.R. Wilson, W. Kobsiriphat, R. Mendoza, H.-Y. Chen, J.M. Hiller, D.J. Miller, K. Thornton, P.W. Voorhees, S.B. Adler, S.A. Barnett, Nat. Mater. 5 (2006) 541–545.

[45] E. Chabert, R. Dendievel, C. Gauthier, J.-Y. Cavaillé, Compos. Sci. Technol. 64 (2004) 309–316.

[46] H. Itoh, T. Yamamoto, M. Mori, T. Horita, N. Sakai, H. Yokokawa, M. Dokiya, J. Electrochem. Soc. 144 (1997) 641–646.

[47] Y. Wang, M.E. Walter, K. Sabolsky, M.M. Seabaugh, Solid State Ionics 177 (2006) 1517–1527.

[48] M. Mori, T. Yamamoto, H. Itoh, H. Inaba, H. Tagawa, J. Electrochem. Soc. 145 (1998) 1374–1381.

[49] J.R. Wilson, S.A. Barnett, Electrochem. Solid-State Lett. 11 (3) (2008) B181–B185.

[50] K.N. Grew, Y.S. Chu, J. Yi, A.A. Peracchio, J.R.I. Jr., Y. Hwu, F.D. Carlo, W.K.S. Chiua, J. Electrochem. Soc. 157 (2010) B783–B792.

[51] H. Iwai, N. Shikazono, T. Matsui, H. Teshima, M. Kishimoto, R. Kishida, D. Hayashi, K. Matsuzaki, D. Kanno, M. Saito, H. Muroyama, K. Eguchi, N. Kasagi, H. Yoshida, J. Power Sources 195 (2010) 955–961.

[52] P.R. Shearing, J. Golbert, R.J. Chater, N.P. Brandon, Chem. Eng. Sci. 64 (17) (2009) 3928–3933.

[53] P.R. Shearing, Q. Cai, J.I. Golbert, V. Yufit, C.S. Adjiman, N.P. Brandon, J. Power Sources 195 (2010) 4804–4810.

[54] A. Wonisch, T. Kraft, M. Moseler, H. Riedel, J. Am. Ceram. Soc. 10 (2009) 1428–1434.

[55] C.L. Martin, D. Bouvard, Int. J. Mech. Sci. 46 (2004) 907–927.